Spatially Resolved Photoexcited Charge-Carrier Dynamics in Phase-Engineered Monolayer MoS_2

Hisato Yamaguchi,[†,#] Jean-Christophe Blancon,[‡,#] Rajesh Kappera,[§] Sidong Lei,[∥] Sina Najmaei,[∥] Benjamin D. Mangum,[⊥] Gautam Gupta,[†] Pulickel M. Ajayan,[∥] Jun Lou,[∥] Manish Chhowalla,[§] Jared J. Crochet,[‡] and Aditya D. Mohite*,[†]

[†]MPA-11 Materials Synthesis and Integrated Devices, Materials Physics and Applications Division and [‡]C-PCS Physical Chemistry and Applied Spectroscopy, Chemistry Division, Los Alamos National Laboratory, Los Alamos, New Mexico 87545, United States, [§]Materials Science and Engineering, Rutgers University, Piscataway, New Jersey 08854, United States, [∥]Materials Science and NanoEngineering, Rice University, Houston, Texas 77005, United States, and [⊥]Pacific Light Technologies, Portland, Oregon 97201, United States. [#]These authors contributed equally to this work.

ABSTRACT A fundamental understanding of the intrinsic optoelectronic properties of atomically thin transition-metal dichalcogenides (TMDs) is crucial for its integration into high performance semiconductor devices. Here, we investigate the transport properties of chemical vapor deposition (CVD) grown monolayer molybdenum disulfide (MoS_2) under photoexcitation using correlated scanning photocurrent microscopy and photoluminescence imaging. We examined the effect of local phase transformation underneath the metal electrodes on the generation of photocurrent across the channel length with diffraction-limited spatial resolution. While maximum photocurrent generation occurs at the Schottky contacts of semiconducting (2H-phase) MoS_2, after the metallic phase transformation (1T-phase), the photocurrent peak is observed toward the center of the device channel, suggesting a strong reduction of native Schottky barriers. Analysis using the bias and position dependence of the photocurrent indicates that the Schottky barrier heights are a few millielectron volts for 1T- and ∼200 meV for 2H-contacted devices. We also demonstrate that a reduction of native Schottky barriers in a 1T device enhances the photoresponsivity by more than 1 order of magnitude, a crucial parameter in achieving high-performance optoelectronic devices. The obtained results pave a way for the fundamental understanding of intrinsic optoelectronic properties of atomically thin TMDs where ohmic contacts are necessary for achieving high-efficiency devices with low power consumption.

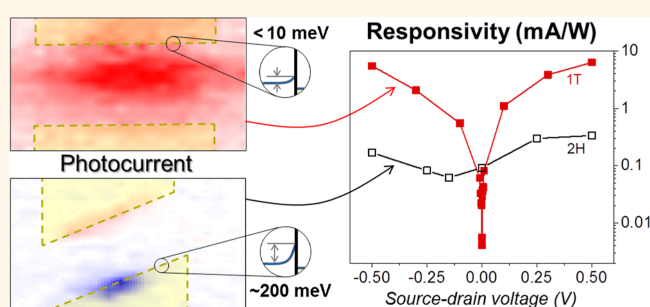

KEYWORDS: MoS_2 · optoelectronic · scanning photocurrent microscopy · contact resistance · phase conversion · monolayer · transition-metal dichalcogenide

Graphene has attracted much attention in recent years due to its true two-dimensional (2D) geometry and one of the highest charge carrier mobility available for any material.[1] The bottleneck of its use in electronic and optoelectronic applications, however, lies in lack of an intrinsic band gap.[2] Graphene-based field effect transistors (FETs) do not turn off completely, and the lifetimes of photoexcited carriers are too short for practical devices due to its semimetallic nature.[3] An emerging class of 2D nanomaterials, which has the complementary properties to that of graphene, is transition-metal dichalcogenides (TMDs). They have intrinsic band gaps in the visible range (1−2 eV) and relatively high charge carrier mobilities (few tens to hundreds of cm^2/V s) that are expected to overcome the limitations of graphene-based optical, electronic, and optoelectronic 2D devices.[4−12] One of the key challenges in this field of research is to achieve ohmic contacts to TMD-based semiconductor devices in order to access intrinsic optoelectronic properties. Schottky contacts provide an extrinsic resistance to current flow and do not allow for a clean measurement of the semiconducting channel performance.[13−15] One accepted process to obtain low-resistance contacts to 2D TMDs such as MoS_2 at present is to use

* Address correspondence to amohite@lanl.gov.

Received for review November 12, 2014 and accepted December 18, 2014.

Published online December 18, 2014
10.1021/nn506469v

© 2014 American Chemical Society

gold and anneal for several days under inert atmosphere.[6,16,17] However, because of time constraints and narrow selection of electrode metals, the breadth of potential applications for TMD-based devices could be limited.

A recent approach in achieving low-resistance contacts is to partially convert the MoS_2 semiconducting (2H) phase into the metallic (1T) phase[18−21] and deposit metal electrodes selectively on the metallic 1T-phase region. We recently demonstrated the application of this phase-engineering approach to obtain high-performance TMD-based FETs *via* formation of low resistance contacts that is independent of the metal used as an electrode.[22,23] Here, we explore the effect of phase-engineered (phase-transformed) contacts on the operation of MoS_2 optoelectronic devices by means of scanning photocurrent microscopy (SPCM)[24−38] correlated with photoluminescence (PL) imaging. More specifically, by comparing the photocurrent profiles along the device channels of the 1T- and 2H-phase contacted devices with/without external bias, we provide a quantitative description of the reduction/elimination of Schottky barriers at the contacts, supported by proposed band diagrams to qualitatively explain the obtained SPCM results. We also analyzed the photoresponsivity of devices, a figure of merit that is critical in designing minority carrier based optoelectronic devices such as solar cells and photodetectors. Our study provides insights into efficient and optimum design of high performance TMD-based devices *via* simple and reliable procedures for forming Ohmic-like contacts to access intrinsic optoelectronic properties.

RESULTS AND DISCUSSION

PL Maps and I−V Characteristics. The photocurrent response of monolayer MoS_2 devices was investigated using the experimental setup illustrated in Figure 1a. Briefly, a chopped 440 nm laser excitation beam is focused on the sample with a spatial resolution of about 350 nm where a galvanometer mirror positioning system allows for surface rastering of the sample to obtain photocurrent maps in SPCM. The photoresponse of the samples was measured by synchronous detection (at the light excitation frequency *f*) of the current at a contact of the device (drain). Devices are biased by applying a voltage potential difference V_{SD} to the other contact electrode (source). Unless otherwise mentioned, the photocurrent response of 2H- and 1T-contacted MoS_2 devices were measured in air under ambient conditions, and with laser excitation powers below 1 μW (<1 kW/cm^2). Both PL and reflection imaging capabilities were used to locate the device positions including the contact electrodes, and were correlated with SPCM results (Supporting Information, Figure S1) (see the Methods). Figure 1b depicts dark current−voltage (*I*−*V*) characteristics of 2H and 1T devices, consistent with our previous investigations.[22,23] Specifically, while typical rectifying behavior due to a formation of Schottky barriers at the contacts was observed for 2H devices (blue line), 1T devices (red line) demonstrated a linear behavior at low applied V_{SD} with enhanced current levels, indicating a strong reduction in the Schottky barrier height (or the formation of ohmic-like contact). PL images of 2H and 1T devices (Figure 1c and d, respectively) show high intensity regions in partial triangular shapes corresponding to monolayer CVD grown MoS_2 sheets, as well as low intensity "cutting" regions indicating the positions of metal electrodes. Dashed green lines highlight the position of the contacts between the MoS_2 channels and electrodes, matching well the optical microscopy images depicted in Figure S1(a) (Supporting Information). PL and optical microscopy surface images show no drastic difference between 2H and 1T devices because phase-converted regions of the latters are fully covered with metal electrodes by design. The devices used in SPCM measurements had channel lengths of about 5 μm (4.88 μm for the 2H device shown in Figure 1c and 5.15 μm for the 1T device in Figure 1d), since shorter channel length led to complexity in data analysis due to merging of photocurrent peaks at the contacts (Supporting Information, Figure S2).

Comparison of Biased SPCM Maps and Line Profiles. SPCM on the 2H-contacted device at zero bias (V_{SD} = 0 V) presents strong photocurrent (I_{ph}) with opposite polarity located near the two contacts at both ends of the device channel (Supporting Information, Figure S3(a)). The result is consistent with the previous report,[39] which describes that the photocurrent primarily originates from the Schottky barriers at the MoS_2/metal contacts. These SPCM features remain largely unchanged under applied bias of V_{SD} = −0.15 V, with the only difference in the amplitude of I_{ph} at each contact and their ratios (Figure 1e). On the contrary, the 1T device at zero bias shows a broad and moderate I_{ph} intensity region near its channel center, in addition to relatively high Schottky photocurrent still observed at the contacts (Supporting Information, Figure S3(b)). At V_{SD} = 0.1 V, in stark contrast to a 2H case, we observe almost complete extinction of the photocurrent peaks at the contacts and the appearance of a broad and high I_{ph} intensity region near the channel center that spans over the entire device area (Figure 1f).

The details of photocurrent evolution *versus* V_{SD} for each case of a 2H and 1T device can be investigated by analyzing the line profiles of the photocurrent I_{ph} across the device, that are taken with increased number of position steps compared to the SPCM maps (between the two electrodes, lines along which the profiles were taken are indicated by gray dotted lines in Figure 1e,f). For a 2H device (Figure 2a), the high I_{ph} intensity regions near the MoS_2/metal contacts (indicated by the red triangle and blue circle) remained at same positions over the entire tested bias range

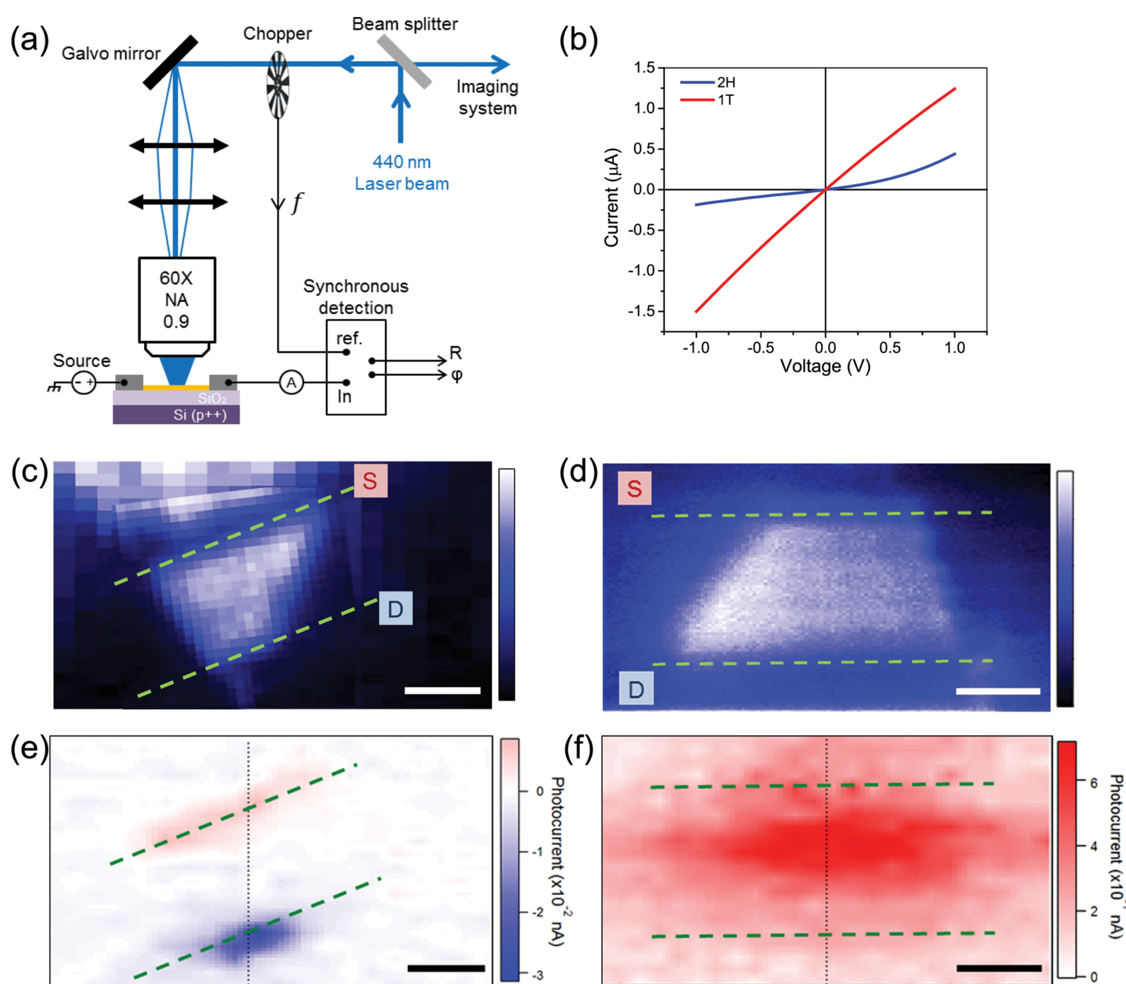

Figure 1. (a) Schematic of the scanning photocurrent microscopy (SPCM) experimental setup used in this study. (b) Dark current−voltage characteristics of 2H- and 1T-contacted devices (blue and red curves, respectively). (c) Photoluminescence (PL) image of a 2H device and (e) its SPCM map under −0.15 V bias. (d) PL image of a 1T device and (f) its SPCM map under 0.1 V bias. Green dashed lines correspond to the position of the contacts between MoS_2 channels and metal electrodes. Photocurrent profiles shown in Figure 2 are measured along the vertical gray dashed lines. S and D boxes indicate the position of the source and drain electrodes, respectively. Scale bars = 3 μm.

(V_{SD} from −0.5 to +0.5 V) while their amplitude increased as V_{SD} increased (yellow regions indicates the position of the electrodes). For a 1T device, on the other hand, high I_{ph} intensity region emerges near the center of the device channel with applied bias, and its amplitude keeps increasing as the voltage increases (Figure 2b, top). The difference between a 2H device case is clear by comparison with the data plotted in the same V_{SD} range (Figure 2b, bottom). Moreover, only few mV of applied V_{SD} was enough to induce the high I_{ph} intensity region in the channel center of a 1T device (Figure 2c). The same observations are drawn from the SPCM maps depicted in the Supporting Information (Figures S4 and S5, corresponding to 2H and 1T devices, respectively). Figure 2d is a comparison of photocurrent I_{ph} amplitude between 1T- and 2H-contacted devices probed at the center of the channels (amplitude of a 2H device is multiplied by 100 for a demonstration purpose). The photocurrent level under bias is much stronger in 1T devices compared to a 2H case, which is consistent with the obtained dark I−V characteristics (Figure 1b). These results clearly demonstrate that a use of devices with 1T contacts over 2H devices allow wider tunability of the active area with enhanced photocurrent response in monolayer MoS_2 based optoelectronic devices. The error bar for photocurrent I_{ph} was higher for a 1T-contacted device compared to a 2H case; however, it was still well below 10%. The larger error bar for a 1T device is possibly due to much reduced Schottky barrier heights at its contacts, which enables a device to be more sensitive to small local potential fluctuations compared to a 2H device.

Schottky Barrier Height Analysis Using SPCM Line Profiles. Analysis of the obtained I_{ph} line profiles can provide insights into quantitative values of Schottky barrier height (SBH) at the contacts. In our analysis, V_{SD} dependence of the photocurrent profiles along the channels of 2H and 1T devices were plotted for the following three signature points: positions near each MoS_2/electrode contacts ($I_{ph,S}$ and $I_{ph,D}$ at the source

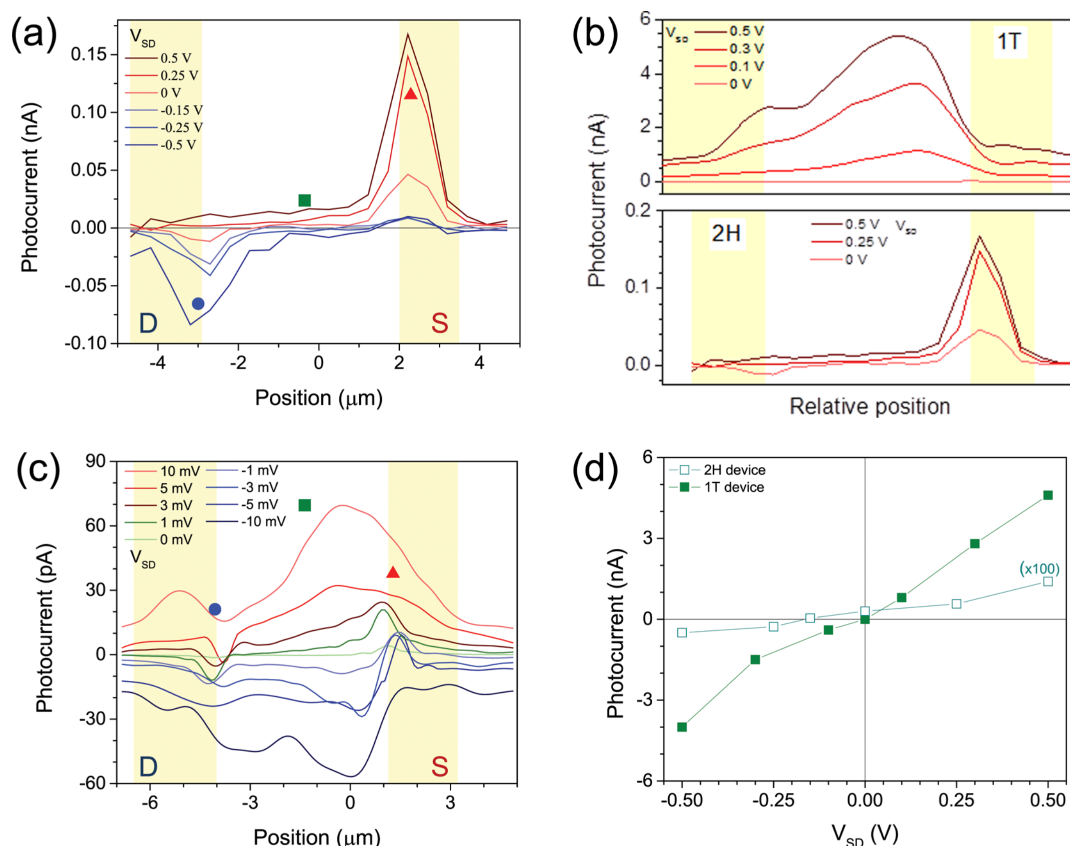

Figure 2. (a) Photocurrent profile along a 2H device channel for different bias V_{SD} in both polarities. Yellow regions indicate the positions of the source (S) or drain (D) contacts. (b) Comparison of photocurrent profiles for 1T- (top) and 2H-contacted devices (bottom) at different V_{SD} (only for positive polarity for simplicity). (c) Photocurrent profile for a 1T device at low V_{SD} (<10 mV) in both polarities. (d) Comparison of photocurrent amplitude between 1T- and 2H-contacted devices at the center of device channels. Amplitude of a 2H device is multiplied by 100 for a demonstration purpose.

and drain electrodes, respectively) and at the center region ($I_{ph,C}$), as indicated by red triangles (source), blue circles (drain), and green squares (center) in parts a and c, respectively, of Figure 2. The results are plotted in Figure 3a for a 2H device (corresponding to Figure 2a I_{ph} profiles) and in Figure 3b for a 1T device (extracted from the I_{ph} response including that of Figure 2c).

In a 2H device case (Figure 3a), $I_{ph,S}$ and $I_{ph,D}$ are nearly symmetric with respect to the origin (I_{ph} = 0 nA and V_{SD} = 0 V), where $I_{ph,S}$ ($I_{ph,D}$) shows almost linear increase of amplitude with positive (negative) V_{SD}. More precisely, extrapolation of $I_{ph,S}$ ($I_{ph,D}$) between +0.5 and −0.15 V (−0.5 and +0.05 V) indicated where a red (blue) dashed line intersects the *Y*-axis (I_{ph} = 0) around −0.21 V (0.21 V), which provides a quantitative estimate of the SBH at the source (drain) contact because the observed change in polarity of I_{ph} at the contacts can be explained by the V_{SD} exceeding their heights of the built-in potential (Schottky barrier).[25,29,30] A further discussion is presented later. The origins of quasipolarity change (not a complete change) observed for $I_{ph,S}$ and $I_{ph,D}$ in our case could be due to external effects such as environmental doping or Fermi level pinning.[13,14] A SBH of ~210 meV, extracted from our SPCM results, is consistent with a true (effective) SBH extracted from variable low-temperature electrical characterization (flat band measurements)[13] that we performed independently using the same electrode metal on MoS_2. The photocurrent at the channel center $I_{ph,C}$ increases monotonically over the entire range of applied bias at a smaller amplitude ($I_{ph,S}$ and $I_{ph,D}$ are measured in the 0.1 nA range, whereas $I_{ph,C}$ operates at a level of 0.01 nA due to absence of a Schottky barrier) and crosses the *Y*-axis around −0.16 V (as indicated by a green line), which is in the range of the intersects observed for $I_{ph,S}$ and $I_{ph,D}$ (gray region on Figure 3a). The agreements between $I_{ph,C}$ intersect and that of the $I_{ph,S}$ and $I_{ph,D}$ can be understood by considering that the $I_{ph,C}$ intersect provides an "average" SBH of the whole device. The slightly different behaviors between the Schottky barriers at each contact are possibly due to a combination of minor difference in the sharpness of the contact MoS_2/electrode interface created during the electrodes deposition[13] and intrinsic/extrinsic inhomogeneity of work function over the MoS_2 surfaces (created during the CVD growth/external environment effects such as water molecule absorptions, respectively).[40,41]

Two major differences observed in a 1T device case (Figure 3b) from that of a 2H case were a 1 order of

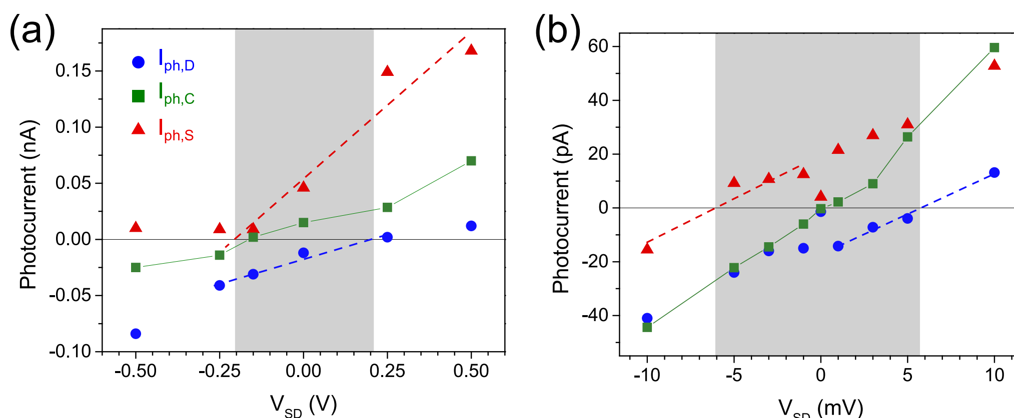

Figure 3. (a, b) Photocurrent amplitude *versus* applied bias V_{SD} at signature points of the profiles in Figure 2a (2H-) and Figure 2c (1T-contacted device), respectively. Gray regions encompass the V_{SD} range, which corresponds to Schottky barriers heights at the source and drain.

magnitude larger total I_{ph} for the same bias range and a *Y*-axis intersect of I_{ph} at almost zero bias. More details of the higher amplitude of I_{ph} will be discussed later, but it is consistent with dark *I*−*V* characteristics (Figure 1b) as mentioned previously for the case of Figure 2d. For a precise determination of *Y*-axis intersect of I_{ph}, I_{ph} at marked three positions (two contacts and center of the device channel) were plotted in much smaller range of bias in Figure 3b (between −10 and +10 mV) compared to a 2H case (Figure 3a). $I_{ph,D}$ and $I_{ph,S}$ cross the *Y*-axis at +5.8 and −6 mV, as indicated with red and blue dashed lines, respectively, providing quantitative values for the reduced SBHs after its 1T-phase transformation (obtained SBH value range is colored in gray). The $I_{ph,C}$ crossed the *Y*-axis at zero (as indicated by a green line) within the resolution of the measurements (<1 mV), which can be interpret as an "average" of source and drain Schottky barriers similar to the case of a 2H device. Note that the obtained value of $I_{ph,C}$ being very close to the average between the two SBHs (−0.1 mV) could be an indication that this particular device had well-balanced source and drain Schottky barriers (having identical heights). The validity of the obtained results was also confirmed on other 1T devices, including the one which we performed photocurrent microscopy at a single position to achieve site-specific SBH values (Supporting Information, Figures S5 and S6). In this case, the SBH was estimated by illuminating the device at a fixed position while sweeping the bias voltage and recording I_{ph} (Supporting Information, Figure S6(b)). Locating the laser spot at an appropriate position near the contact allows a determination of SBH with improved accuracy (spatial and energy) with shorter measurement time compared to the line or map scan counterparts. Analysis of the data yields ∼0.05 and ∼0.46 meV for the drain and source SBH, respectively, reaffirming the strong reduction of SBH after a phase transformation to 1T. The photocurrent at the channel center crosses the *Y*-axis at ∼0.37 mV, indicating that the source Schottky barrier dominates the response of this particular device at small bias range due to its larger amplitude compared to the drain. All SBH values we obtained for 1T devices are up to 2−3 orders of magnitude lower than a 2H device case, quantitatively demonstrating the strong reduction of native SBH and hence the formation of nearly ohmic-like contacts for monolayer MoS_2 using the phase engineering approach (*i.e.*, by converting of the MoS_2 2H-phase into 1T-phase underneath the contact electrodes). Note that an obtained SBH of few meV or lower for 1T-contacted device does not consider a contribution from thermal energy (∼25 meV at room temperature). The obtained SBH, therefore may better be described as a voltage necessary to drive carriers to the contacts. However, this does not affect our conclusion of a 1T device having strongly reduced SBH compared to a 2H case because the experimental uncertainty can only be ∼25 meV at the most. Furthermore, an effect of illumination intensity on a determination of SBH should be negligible in this study, unlike a case of open circuit voltage V_{OC} for organic photovoltaics. This is due to 4 orders of magnitude higher carrier mobility in our MoS_2 (∼10 $cm^2/(V\ s)$)[22,23] compared to that of an organic photovoltaic system (∼10^{-3} $cm^2/(V\ s)$),[42] which reduces the degree of illumination intensity dependence on SBH by at least several orders of magnitude (see the Supporting Information, S7, for details).[43,44]

Insights into Potential Profile across Devices. Complementary qualitative analysis of the Schottky barriers was obtained by plotting the integrated photocurrent along the devices channels (Figure 4a,b derived from Figure 2a, including that of part c, respectively; see also the Supporting Information, Figure S7), that provides insight into potential profile of 2H and 1T devices. Although this method does not provide direct access to the intrinsic potential profile across the device as suggested in ref 45, it offers useful qualitative

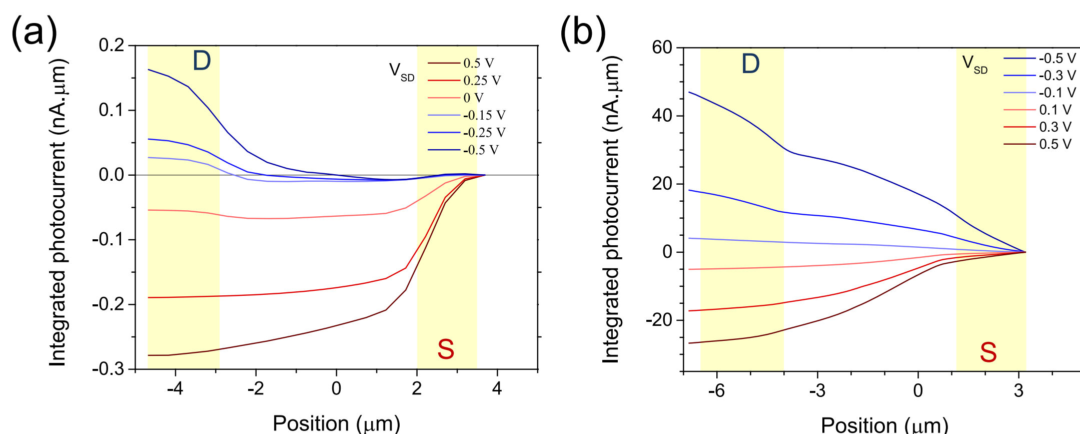

Figure 4. Integrated photocurrent along (a) 2H and (b) 1T device channels for different applied bias V_{SD}.

information on the relative evolution of the potential profile depending on the applied bias. In a 2H device case (Figure 4a and Supporting Information, Figure S7(a)), strong variations of the potential profiles take place at the source (drain) contact position for positive (negative) bias, indicating strong build-in local electric field drives the separation of charges, thus enhancing the photocurrent. The results are in agreement with formation of SBH at the contact as observed in Figures 2a and 3a. On the other hand, a 1T device (Figure 3b and Supporting Information, Figure S7(b)) shows a much smoother potential modulation across the device channel. These observations validate the absence of significant build-in field along the channel and confirm the strong attenuation of the Schottky barriers in 1T devices, as quantitatively discussed above.

Photocurrent Generation Mechanism. Parts a–d of Figure 5 illustrate a possible mechanism that explains the observed photocurrent generation in 2H- and 1T-contacted devices of monolayer MoS_2. Specifically, the conduction and valence band potential profiles across the device channel are drawn along with our interpretation of the charge diffusion, in correlation with the schematics of the photocurrent line profiles achieved in the SPCM. For our explanations, we classified the generated photocurrent into the following two dominant types; a Schottky barrier driven photocurrent located at MoS_2/electrode contacts (noted I_{SC}), and a combination of all the other types of photocurrent I_{PC}[38,45−48] (most likely dominated by photoconductive photocurrent as indicated in ref 48). We suspect that a thermoelectric effect has only a minor contribution to our observed overall photocurrent as confirmed by recent studies (details are provided in the Supporting Information, S9).[39,48] At zero bias (V_{SD} = 0 V) and under illumination, 2H and 1T devices yield dominant photocurrent I_{SC} at both source and drain contacts due to the presence of Schottky barriers. These Schottky barriers generate a local built-in electric field that separate the photoexcited carriers at the contacts (residue SBH for 1T case) and drives the hole (electron) carriers toward (away from) the closest electrode (carrier flows depicted by red arrows in Figure 5a,c). The depletion width of the Shottky barrier is much smaller than the spatial resolution of our SPCM setup (∼50 nm[45] *versus* few hundreds of nm) and this results in relatively narrow high intensity peak at the contacts. Moreover, the amplitude of the photocurrent generated at the contacts is determined by the amplitudes of SBH thus resulting in higher I_{SC} for a 2H case compared to a 1T case (parts a and c, respectively, of Figure 5, respectively). This is consistent with our SPCM results without any bias (V_{SD} = 0 V) that yielded 1 order of magnitude higher I_{ph} for a 2H device compared to a 1T device due to the difference in their SBH (∼200 meV and <10 meV for 2H and 1T, respectively). On the other hand, the photoexcited carriers located further away from the contacts/toward center region of a 2H device do not contribute to I_{ph} due to lack of a driving potential. In a 1T device, however, the moderate number of photogenerated carriers can reach the electrodes due to absence/reduction of potential barriers at the contacts and contribute to photocurrent I_{ph} observed at the device channel center. This interpretation suggests that the broad and moderate I_{ph} feature in the center of the device can be used as an important indication of dramatic reduction of the Schottky barrier.

Under a bias, in a positive case, for example, abovementioned phenomena appears to be pronounced and emphasizes the differences in SPCM response between 2H and 1T devices (the same analysis is possible for negative bias case by exchange of source and drain contacts). In a 2H device (Figure 5b), applied external field affects the SBH at the both contacts. On the source, it enables carriers that are generated at positions further away from the source to reach electrodes (source for holes and drain for electrons) and contribute to I_{SC} as indicated by longer red arrows. On the drain, however, it decreases I_{SC} at the drain

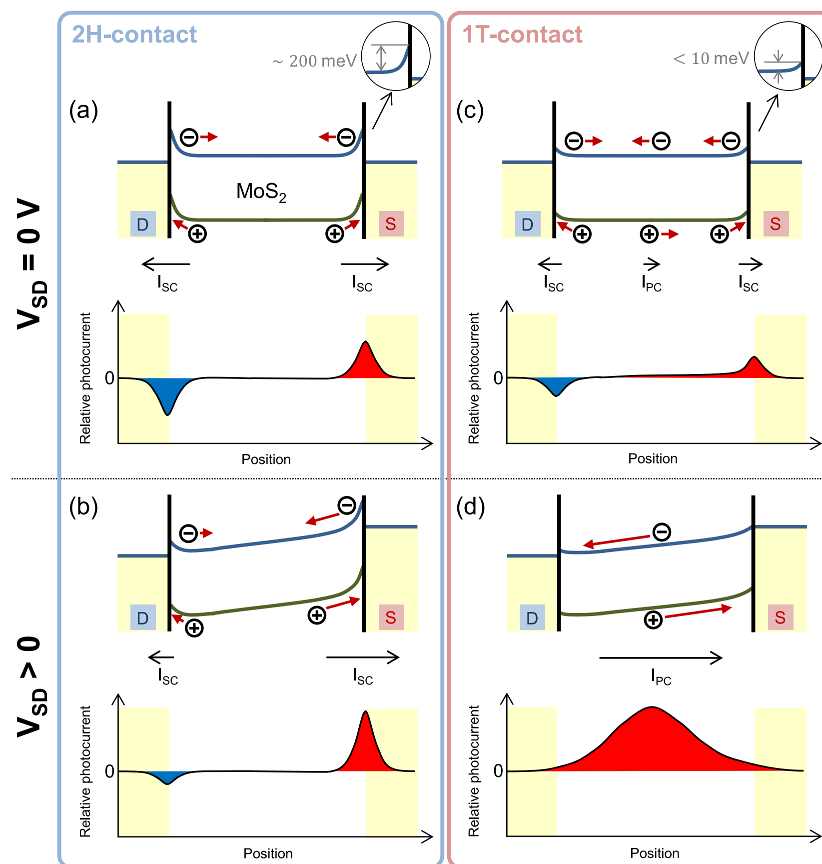

Figure 5. Proposed mechanisms of photocurrent generation in (a, b) 2H-contacted and (c, d) 1T-contacted devices. Top panels (a), (c) and bottom ones (b), (d) correspond to situations at zero and positive bias, respectively. In each panel, the top schematic illustrates the conduction (blue) and valence (green) bands variations along the device channel; the MoS_2 monolayer is sandwiched between the two metal electrodes (positions of the electrodes are shown in yellow, with S and D corresponding to the source and drain, respectively). Insets illustrated enlarged MoS_2/electrode contact and depict the Schottky barrier height derived from our SPCM measurements. Diffusion of electrons (−) and holes (+) are represented by red arrows, and the corresponding plot schematics for relative photocurrent *versus* the position along the channel are illustrated below. The direction and relative amplitude of currents are indicated by arrows in-between the two schemes, with I_{SC} indicating the photocurrent generated by the Schottky barriers and I_{PC} indicating photocurrent, which is a sum of all the other types.

contact in relative to the source due to decreased SBH (indicated by shorter arrows). Positions of high I_{SC} regions remain unchanged. It should be noted that this analysis is valid in a bias range that is away from the saturation regime of the device, and 0.5 V used in our case is well below the critical voltage.[23] In 1T devices, the elimination effect of Schottky barriers becomes even more apparent upon applying an extremely small bias of few millivolts (Figure 5d). The tilt/bending of the band potential rapidly enable photoexcited carriers to overcome the SBH at both contacts and render I_{SC} negligible (the peaks located at the contacts disappear). This allows for uninhibited flow of photoexcited carriers even under very small external electric-fields unlike in the case of 2H-contacted devices. As a result, I_{PC} maximized near the center of the channel emerges and spans over the entire device. This would not be possible with 2H-contacted device because a formation of Schottky barriers at the electrodes hinders electrons from reaching the electrodes, resulting in no observable total photocurrent I_{ph} (Figure 5b). The gate dependence of SPCM results is expected to provide further insights into the evolution of Schottky barrier heights and detailed photogeneration mechanism in MoS_2 based devices, and should be investigated in future works.

Device Performance. Integrated photocurrent response along device channels (Figure 6a) and the local photoresponsivity (Figure 6b) demonstrate the enhanced performances of 1T-contacted devices in comparison to their 2H counterparts. We observe same trends in the integrated photocurrent and dark current variations as a function of the bias (Figure 2a) as well as comparable ratio of current amplitudes between the 2H and 1T devices (about 1 order of magnitude difference). This is consistent with the trend of 133% carrier mobility increase observed for 1T device FETs in our previous reports.[22,23] Moreover, a 1T device presents photoresponsivity R (ratio of the local I_{ph} to the excitation power) about 30 times larger (R = 5.5 mA/W)

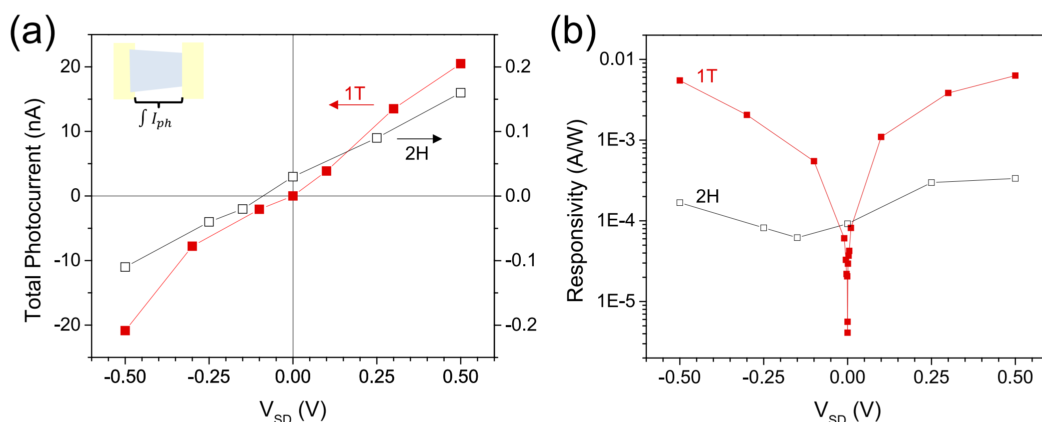

Figure 6. 2H- vs 1T-contacted devices performances and their evolution with applied source-drain bias V_{SD}. (a) Total photocurrent integrated over the channel length of 2H (black dots, right scale) and 1T (red squares, left scale) devices. (b) Local photoresponsivity extracted from the SPCM measurements as the ratio of maximum photocurrent to the excitation power.

than a 2H device case (R = 0.2 mA/W) at V_{SD} = −0.5 V. A 2H device responsivity is almost invariant over the whole V_{SD} bias range of −0.5 to 0.5 V, in agreement with the fact that I_{SC} (Schottky barriers driven photocurrent) dominates the photoresponse. On the contrary, a 1T device shows strong responsivity variations in a V-shape centered at $V_{SD} \approx 0$, where R presents a drastic increase as V_{SD} overcome the SBH (photocurrent regime changes from I_{SC} at low bias (−10 mV ≤ V_{SD} ≤ 10 mV) to I_{PC}). The responsivity R = 6.3 mA/W at V_{SD} = 0.5 V (excitation power 0.7 μW at 2.8 eV (440 nm)) is larger than observations in monolayer graphene transistors[47] and comparable to recent reports in monolayer MoS_2 under similar operation parameters.[48−50] We expect further enhancement with illumination at the excitonic absorption states.[5] Our results demonstrate effectiveness of using the phase engineering approach (conversion of 2H- to 1T-phase) for monolayer MoS_2 to eliminate the Schottky barriers at the contacts, thus improving the operating current level as well as increasing the net active area of the device throughout the entire channel to achieve high performance 2D optoelectronic devices.

CONCLUSION

In conclusion, we performed SPCM on monolayer MoS_2 individual sheet devices with phase-engineered contacts and compared the results with conventionally used 2H-contacted devices. The results revealed that in addition to the increased photocurrent level, the active area of monolayer MoS_2 optoelectronic devices broadened over their entire area due to Schottky barrier elimination of a 1T device. This is in stark contrast to narrow active regions near the electrodes for a 2H device. Furthermore, analysis of SPCM results indicated that the Schottky barrier heights (SBH) at the contacts of a 1T device is reduced by at least 1 order of magnitude compared to a 2H case, from ∼200 meV down to few meV or even lower. Our proposed model suggests that this elimination of Schottky barriers at the electrodes achieved by the conversion of semiconducting 2H-phase to metallic 1T-phase is responsible for the observed broadening of the active area and increase of photocurrent level. We also demonstrated that the photoresponsivity increases by more than an order of magnitude for a 1T device compared to a 2H case, a promising indication toward high performance optoelectronic devices. Our results pave a pathway for the design of high performance TMD-based 2D optoelectronic devices and fundamental understanding of their optoelectronic properties.

METHODS

Fabrication Procedures of 1T- and 2H-Phase Contacted MoS_2 Devices. Monolayer CVD MoS_2 sheets[40] were transferred[51] onto degenerately p-doped (R < 0.0015Ω-cm) patterned silicon substrates capped with 100 nm oxide layer. Statically dispensed PMMA (A4, Microchem Corp.) was spin coated onto the sample at 4000 rpm for 60 s and was followed by prebaking at 180 °C for 90 s. For fabrications of 1T-phase contact devices, two separate lithography processes were performed. In the first lithography step, electrode windows were opened on the MoS_2 sheet using conventional e-beam lithography. After opening the electrode windows, we exposed the samples to *n*-butyllithium (1.6M, Sigma-Aldrich) for 48 h and then cleaned them with hexane.[22,23] All butyllithium exposure was conducted in an argon-filled glovebox. Samples were then cleaned with deionized water in order to remove residual lithium on MoS_2. This was followed by PMMA etching using HPLC grade acetone (Fisher Scientific), followed by a 2-propanol rinse. PMMA was again spin coated following the same recipe as described earlier. A second lithography step was performed to open the electrode windows at the same regions as described earlier.

We performed e-beam evaporation to deposit titanium (5 nm) and gold (50 nm) under high vacuum conditions of 10^{-7} Torr at a slow deposition rate of 1 Å/s. This was followed by lift off using acetone after which the samples were properly rinsed with 2-propanol to eliminate acetone residue followed

by blow drying with compressed nitrogen gas. For fabrications of conventional 2H-phase contact devices, metal electrodes were deposited without *n*-butyllithium exposure steps.

Scanning Photocurrent Microscopy (SPCM) and Photoluminescence (PL) Measurements. For SPCM measurements, 440 nm pulsed excitation light was delivered by a laser diode (PicoQuant) and focused on the sample by a 60× Olympus objective with 0.9 numerical aperture to be scanned over the samples in a form of map/line/fixed position by means of a galvanometer mirror positioning system and two lenses arranged in a 4f-configuration.[34] As illustrated in Figure 1a, synchronous detection was achieved *via* SR-830 lock-in amplifier (Stanford Research Systems) using the reference frequency input from the chopper (~370 Hz). The photocurrent signal was first amplified by a SR-570 current amplifier (Stanford Research Systems), and the AC component of the output voltage signal was used as direct input to the lock-in amplifier. Both the amplitude R and the phase φ of the photocurrent were monitored and analyzed. Correlated PL and/or reflected light obtained for the same position of SPCM map was detected using an avalanche photodiode and a silicon photodiode, respectively, allowing determination of the exact location of monolayer MoS_2 sheet devices and the contact electrodes.

Conflict of Interest: The authors declare no competing financial interest.

Acknowledgment. We acknowledge S. E. Yalcin of Los Alamos National Laboratory (LANL) for the technical support and J. A. Garcia of LANL for the administrative support at the initial stage of SPCM system setup. We also acknowledge J. K. Baldwin of LANL for metal electrode depositions, D. J. William of LANL for maintenance of the SEM system for e-beam lithography, and W. Nie of LANL for fruitful discussions. H.Y. acknowledges financial support from a LANL Director's Postdoctoral Fellowship and S. K. Doorn of LANL for initial support as a host. This work was financially supported by the LANL Laboratory Directed Research and Development (LDRD) program and was performed, in part, at the Center for Integrated Nanotechnologies, an Office of Science User Facility operated for the U.S. Department of Energy (DOE) Office of Science by Los Alamos National Laboratory (Contract No. DE-AC52-06NA25396) and Sandia National Laboratories (Contract No. DE-AC04-94AL85000).

Supporting Information Available: Optical, reflection, and PL images for determination of device positions, SPCM on short channel length devices, amplitude and phase information extracted from SPCM maps, bias-dependent SPCM maps of a 2H-contacted device, reproducibility of bias-dependent SPCM maps of a 1T-contacted device, fixed position photocurrent microscopy of a 1T-contacted device, effects of illumination intensity on SBH determinations, photocurrent integrated from opposite direction, and thermoelectric effect contributions in photocurrents measured in this study. This material is available free of charge *via* the Internet at http://pubs.acs.org.

REFERENCES AND NOTES

1. Novoselov, K. S.; Geim, A. K.; Morozov, S. V.; Jiang, D.; Zhang, Y.; Dubonos, S. V.; Grigorieva, I. V.; Firsov, A. A. Electric Field Effect in Atomically Thin Carbon Films. *Science* **2004**, *306*, 666–669.
2. Ohta, T.; Bostwick, A.; Seyller, T.; Horn, K.; Rotenberg, E. Controlling the Electronic Structure of Bilayer Graphene. *Science* **2006**, *313*, 951–954.
3. Novoselov, K. S.; Falko, V. I.; Colombo, L.; Gellert, P. R.; Schwab, M. G.; Kim, K. A Roadmap for Graphene. *Nature* **2012**, *490*, 192–200.
4. Splendiani, A.; Sun, L.; Zhang, Y.; Li, T.; Kim, J.; Chim, C.-Y.; Galli, G.; Wang, F. Emerging Photoluminescence in Monolayer MoS_2. *Nano Lett.* **2010**, *10*, 1271–1275.
5. Mak, K. F.; Lee, C.; Hone, J.; Shan, J.; Heinz, T. F. Atomically Thin MoS_2: A New Direct-Gap Semiconductor. *Phys. Rev. Lett.* **2010**, 105.
6. Radisavljevic, B.; Radenovic, A.; Brivio, J.; Giacometti, V.; Kis, A. Single-Layer MoS_2 Transistors. *Nat. Nanotechnol.* **2011**, *6*, 147–150.
7. Wang, Q. H.; Kalantar-Zadeh, K.; Kis, A.; Coleman, J. N.; Strano, M. S. Electronics and Optoelectronics of Two-Dimensional Transition Metal Dichalcogenides. *Nat. Nanotechnol.* **2012**, *7*, 699–712.
8. Nicolosi, V.; Chhowalla, M.; Kanatzidis, M. G.; Strano, M. S.; Coleman, J. N. Liquid Exfoliation of Layered Materials. *Science* **2013**, 340.
9. Chhowalla, M.; Shin, H. S.; Eda, G.; Li, L. J.; Loh, K. P.; Zhang, H. The Chemistry of Two-Dimensional Layered Transition Metal Dichalcogenide Nanosheets. *Nat. Chem.* **2013**, *5*, 263–275.
10. Jariwala, D.; Sangwan, V. K.; Late, D. J.; Johns, J. E.; Dravid, V. P.; Marks, T. J.; Lauhon, L. J.; Hersam, M. C. Band-like Transport in High Mobility Unencapsulated Single-Layer MoS_2 Transistors. *Appl. Phys. Lett.* **2013**, *102*, 173107.
11. Jariwala, D.; Sangwan, V. K.; Lauhon, L. J.; Marks, T. J.; Hersam, M. C. Emerging Device Applications for Semiconducting Two-Dimensional Transition Metal Dichalcogenides. *ACS Nano* **2014**, *8*, 1102–1120.
12. Lei, S.; Ge, L.; Najmaei, S.; George, A.; Kappera, R.; Lou, J.; Chhowalla, M.; Yamaguchi, H.; Gupta, G.; Vajtai, R.; *et al.* Evolution of the Electronic Band Structure and Efficient Photo-Detection in Atomic Layers of InSe. *ACS Nano* **2014**, *8*, 1263–1272.
13. Das, S.; Chen, H.-Y.; Penumatcha, A. V.; Appenzeller, J. High Performance Multilayer MoS_2 Transistors with Scandium Contacts. *Nano Lett.* **2012**, *13*, 100–105.
14. Liu, H.; Neal, A. T.; Ye, P. D. Channel Length Scaling of MoS_2 MOSFETs. *ACS Nano* **2012**, *6*, 8563–8569.
15. Liu, H.; Si, M.; Deng, Y.; Neal, A. T.; Du, Y.; Najmaei, S.; Ajayan, P. M.; Lou, J.; Ye, P. D. Switching Mechanism in Single-Layer Molybdenum Disulfide Transistors: An Insight into Current Flow across Schottky Barriers. *ACS Nano* **2013**, *8*, 1031–1038.
16. Baugher, B. W. H.; Churchill, H. O. H.; Yang, Y.; Jarillo-Herrero, P. Intrinsic Electronic Transport Properties of High-Quality Monolayer and Bilayer MoS_2. *Nano Lett.* **2013**, *13*, 4212–4216.
17. Schmidt, H.; Wang, S.; Chu, L.; Toh, M.; Kumar, R.; Zhao, W.; Castro Neto, A. H.; Martin, J.; Adam, S.; Özyilmaz, B.; *et al.* Transport Properties of Monolayer MoS_2 Grown by Chemical Vapor Deposition. *Nano Lett.* **2014**, *14*, 1909–1913.
18. Eda, G.; Yamaguchi, H.; Voiry, D.; Fujita, T.; Chen, M.; Chhowalla, M. Photoluminescence from Chemically Exfoliated MoS_2. *Nano Lett.* **2011**, *11*, 5111–5116.
19. Eda, G.; Fujita, T.; Yamaguchi, H.; Voiry, D.; Chen, M.; Chhowalla, M. Coherent Atomic and Electronic Heterostructures of Single-Layer MoS_2. *ACS Nano* **2012**, *6*, 7311–7317.
20. Voiry, D.; Yamaguchi, H.; Li, J. W.; Silva, R.; Alves, D. C. B.; Fujita, T.; Chen, M. W.; Asefa, T.; Shenoy, V. B.; Eda, G.; *et al.* Enhanced Catalytic Activity in Strained Chemically Exfoliated WS_2 Nanosheets for Hydrogen Evolution. *Nat. Mater.* **2013**, *12*, 850–855.
21. Voiry, D.; Salehi, M.; Silva, R.; Fujita, T.; Chen, M.; Asefa, T.; Shenoy, V. B.; Eda, G.; Chhowalla, M. Conducting MoS_2 Nanosheets as Catalysts for Hydrogen Evolution Reaction. *Nano Lett.* **2013**, *13*, 6222–6227.
22. Kappera, R.; Voiry, D.; Yalcin, S. E.; Branch, B.; Gupta, G.; Mohite, A. D.; Chhowalla, M. Phase-Engineered Low-Resistance Contacts for Ultrathin MoS_2 Transistors. *Nat. Mater.* **2014**, *13*, 1128–1134.
23. Kappera, R.; Voiry, D.; Yalcin, S. E.; Jen, W.; Acerce, M.; Torrel, S.; Branch, B.; Lei, S.; Chen, W.; Najmaei, S.; *et al.* Metallic 1T Phase Source/Drain Electrodes for Field Effect Transistors from Chemical Vapor Deposited MoS_2. *APL Mater.* **2014**, *2*, 092516.
24. Freitag, M.; Martin, Y.; Misewich, J. A.; Martel, R.; Avouris, P. Photoconductivity of Single Carbon Nanotubes. *Nano Lett.* **2003**, *3*, 1067–1071.
25. Ahn, Y.; Dunning, J.; Park, J. Scanning Photocurrent Imaging and Electronic Band Studies in Silicon Nanowire Field Effect Transistors. *Nano Lett.* **2005**, *5*, 1367–1370.
26. Gu, Y.; Romankiewicz, J. P.; David, J. K.; Lensch, J. L.; Lauhon, L. J. Quantitative Measurement of the Electron and Hole

Mobility-Lifetime Products in Semiconductor Nanowires. *Nano Lett.* **2006**, *6*, 948–952.
27. Mohite, A.; Lin, J.-T.; Sumanasekera, G.; Alphenaar, B. W. Field-Enhanced Photocurrent Spectroscopy of Excitonic States in Single-Wall Carbon Nanotubes. *Nano Lett.* **2006**, *6*, 1369–1373.
28. Ahn, Y. H.; Tsen, A. W.; Kim, B.; Park, Y. W.; Park, J. Photocurrent Imaging of p-n Junctions in Ambipolar Carbon Nanotube Transistors. *Nano Lett.* **2007**, *7*, 3320–3323.
29. Freitag, M.; Tsang, J. C.; Bol, A.; Yuan, D.; Liu, J.; Avouris, P. Imaging of the Schottky Barriers and Charge Depletion in Carbon Nanotube Transistors. *Nano Lett.* **2007**, *7*, 2037–2042.
30. Lee, E. J. H.; Balasubramanian, K.; Dorfmüller, J.; Vogelgesang, R.; Fu, N.; Mews, A.; Burghard, M.; Kern, K. Electronic-Band-Structure Mapping of Nanotube Transistors by Scanning Photocurrent Microscopy. *Small* **2007**, *3*, 2038–2042.
31. Mueller, T.; Xia, F.; Freitag, M.; Tsang, J.; Avouris, P. Role of Contacts in Graphene Transistors: A Scanning Photocurrent Study. *Phys. Rev. B* **2009**, *79*, 245430.
32. Mohite, A. D.; Santos, T. S.; Moodera, J. S.; Alphenaar, B. W. Observation of the Triplet Exciton in EuS-Coated Single-Walled Nanotubes. *Nat. Nanotechnol.* **2009**, *4*, 425–429.
33. Sun, D.; Aivazian, G.; Jones, A. M.; Ross, J. S.; Yao, W.; Cobden, D.; Xu, X. Ultrafast Hot-Carrier-Dominated Photocurrent in Graphene. *Nat. Nanotechnol.* **2012**, *7*, 114–118.
34. Mohite, A. D.; Perea, D. E.; Singh, S.; Dayeh, S. A.; Campbell, I. H.; Picraux, S. T.; Htoon, H. Highly Efficient Charge Separation and Collection across *in Situ* Doped Axial VLS-Grown Si Nanowire p-n Junctions. *Nano Lett.* **2012**, *12*, 1965–1971.
35. Yang, Y.; Li, J.; Wu, H.; Oh, E.; Yu, D. Controlled Ambipolar Doping and Gate Voltage Dependent Carrier Diffusion Length in Lead Sulfide Nanowires. *Nano Lett.* **2012**, *12*, 5890–5896.
36. Jariwala, D.; Sangwan, V. K.; Wu, C.-C.; Prabhumirashi, P. L.; Geier, M. L.; Marks, T. J.; Lauhon, L. J.; Hersam, M. C. Gate-Tunable Carbon Nanotube-MoS_2 Heterojunction p-n Diode. *Proc. Nat. Acad. Sci.* **2013**, *110*, 18076–18080.
37. DeBorde, T.; Aspitarte, L.; Sharf, T.; Kevek, J. W.; Minot, E. D. Photothermoelectric Effect in Suspended Semiconducting Carbon Nanotubes. *ACS Nano* **2013**, *8*, 216–221.
38. Graham, R.; Yu, D. Scanning Photocurrent Microscopy in Semiconductor Nanostructures. *Mod. Phys. Lett. B* **2013**, *27*, 1330018.
39. Wu, C.-C.; Jariwala, D.; Sangwan, V. K.; Marks, T. J.; Hersam, M. C.; Lauhon, L. J. Elucidating the Photoresponse of Ultrathin MoS_2 Field-Effect Transistors by Scanning Photocurrent Microscopy. *J. Phys. Chem. Lett.* **2013**, *4*, 2508–2513.
40. Najmaei, S.; Liu, Z.; Zhou, W.; Zou, X. L.; Shi, G.; Lei, S. D.; Yakobson, B. I.; Idrobo, J. C.; Ajayan, P. M.; Lou, J. Vapour Phase Growth and Grain Boundary Structure of Molybdenum Disulphide Atomic Layers. *Nat. Mater.* **2013**, *12*, 754–759.
41. Najmaei, S.; Zou, X.; Er, D.; Li, J.; Jin, Z.; Gao, W.; Zhang, Q.; Park, S.; Ge, L.; Lei, S.; *et al.* J. Tailoring the Physical Properties of Molybdenum Disulfide Monolayers by Control of Interfacial Chemistry. *Nano Lett.* **2014**, *14*, 1354–1361.
42. Garcia-Belmonte, G.; Munar, A.; Barea, E. M.; Bisquert, J.; Ugarte, I.; Pacios, R. Charge Carrier Mobility and Lifetime of Organic Bulk Heterojunctions Analyzed by Impedance Spectroscopy. *Org. Electron.* **2008**, *9*, 847–851.
43. Koster, L. J. A.; Mihailetchi, V. D.; Blom, P. W. M. Bimolecular Recombination in Polymer/Fullerene Bulk Heterojunction Solar Cells. *Appl. Phys. Lett.* **2006**, *88*, 052104.
44. Wetzelaer, G.-J. A. H.; Van der Kaap, N. J.; Koster, L. J. A.; Blom, P. W. M. Quantifying Bimolecular Recombination in Organic Solar Cells in Steady State. *Adv. Energy Mater.* **2013**, *3*, 1130–1134.
45. Fu, D.; Zou, J.; Wang, K.; Zhang, R.; Yu, D.; Wu, J. Electrothermal Dynamics of Semiconductor Nanowires under Local Carrier Modulation. *Nano Lett.* **2011**, *11*, 3809–3815.
46. Buscema, M.; Barkelid, M.; Zwiller, V.; van der Zant, H. S. J.; Steele, G. A.; Castellanos-Gomez, A. Large and Tunable Photothermoelectric Effect in Single-Layer MoS_2. *Nano Lett.* **2013**, *13*, 358–363.
47. Freitag, M.; Low, T.; Xia, F.; Avouris, P. Photoconductivity of Biased Graphene. *Nat. Photonics* **2013**, *7*, 53–59.
48. Furchi, M. M.; Polyushkin, D. K.; Pospischil, A.; Mueller, T. Mechanisms of Photoconductivity in Atomically Thin MoS_2. *Nano Lett.* **2014**, *14*, 6165–6170.
49. Yin, Z.; Li, H.; Li, H.; Jiang, L.; Shi, Y.; Sun, Y.; Lu, G.; Zhang, Q.; Chen, X.; Zhang, H. Single-Layer MoS_2 Phototransistors. *ACS Nano* **2012**, *6*, 74–80.
50. Choi, W.; Cho, M. Y.; Konar, A.; Lee, J. H.; Cha, G.-B.; Hong, S. C.; Kim, S.; Kim, J.; Jena, D.; Joo, J.; *et al.* High-Detectivity Multilayer MoS_2 Phototransistors with Spectral Response from Ultraviolet to Infrared. *Adv. Mater.* **2012**, *24*, 5832–5836.
51. Reina, A.; Son, H.; Jiao, L.; Fan, B.; Dresselhaus, M. S.; Liu, Z.; Kong, J. Transferring and Identification of Single- and Few-Layer Graphene on Arbitrary Substrates. *J. Phys. Chem. C* **2008**, *112*, 17741–17744.